

# Ab Initio Simulations of the Kinetic Properties of the Hydrogen Monomer on Graphene<sup>†</sup>

Liang Feng Huang,<sup>‡</sup> Mei Yan Ni,<sup>\*,§</sup> Xiao Hong Zheng,<sup>‡</sup> Wang Huai Zhou,<sup>‡</sup> Yong Gang Li,<sup>‡</sup> and Zhi Zeng<sup>\*,‡</sup>

Key Laboratory of Materials Physics, Institute of Solid State Physics, Chinese Academy of Sciences, Hefei 230031, China, and School of Electronic Science and Applied Physics, Hefei University of Technology, Hefei 230009, China

Received: September 25, 2010; Revised Manuscript Received: November 11, 2010

The understanding of the kinetic properties of hydrogen (isotopes) adatoms on graphene is important in many fields. The kinetic properties of hydrogen-isotope (H, D, and T) monomers were simulated using a composite method consisting of density functional theory, density functional perturbation theory, and harmonic transition state theory. The kinetic changes of the magnetic property and the aromatic  $\pi$  bond of the hydrogenated graphene during the desorption and diffusion of the hydrogen monomer were discussed. The vibrational zero-point energy corrections in the activation energies were found to be significant ranging from 0.072 to 0.205 eV. The results obtained from quantum mechanically modified harmonic transition state theory were compared with the ones obtained from classical-limit harmonic transition state theory over a wide temperature range. The phonon spectra of hydrogenated graphene were used to closely explain the (reversed) isotope effects in the prefactor, the activation energy, and the jump frequency of the hydrogen monomer. The kinetic properties of the hydrogen-isotope monomers were simulated under conditions of annealing for 10 min and of heating at a constant rate (1.0 K/s). The isotope effect was observed; that is, a hydrogen monomer of lower mass is desorbed and diffuses more easily (with lower activation energies). The results presented herein are very similar to other reported experimental observations. This study of the kinetic properties of the hydrogen monomer and many other involved implicit mechanisms provides a better understanding of the interaction between hydrogen and graphene.

## I. Introduction

The fact that hydrogen interacts with graphite surface in outer space<sup>1–4</sup> and in fusion devices<sup>4,5</sup> requires a clear understanding of the kinetic properties of hydrogen adatoms on graphite surfaces for astronomy and the nuclear industry. Such properties are also very important for the realization of both graphite-based hydrogen storage<sup>6</sup> and graphene-based electronics.<sup>7–15</sup>

The desorption and diffusion of hydrogen adatoms on graphite surfaces are two important kinetic processes whose properties depend sensitively on the interaction between the adatom and the graphite surface. Consequently, investigation of the desorption and diffusion of hydrogen adatoms on graphite surfaces can further our understanding of the mechanisms involved in these interactions. Some research has been carried out on the kinetic properties of hydrogen adatoms on graphite surfaces.<sup>2,3,16,17</sup> The adsorption of hydrogen monomers on graphene is an essential step in hydrogenation, and the kinetic properties of this step determine the outcome of the hydrogenation process. Hornekær et al. found that a large fraction of the D monomers on a graphite surface will be desorbed during annealing at room temperature for 10 min, while the D monomers on the graphite surface are diffusionally immobile at room temperature.<sup>3</sup> Such diffusional immobility is consistent with Baouche's observations in time-programmed desorption experiments.<sup>18</sup> Some theoretical studies on the kinetic properties of hydrogen monomers have also been reported.<sup>3,4,19–22</sup> The calculated chemisorption energies

of hydrogen monomer on graphene vary around a value of 0.75 eV with a range of about 0.3 eV; this magnitude of variation represents quite a large energetic uncertainty in kinetics. Furthermore, in kinetic simulations, the vibrational characteristics of the light-mass hydrogen monomers should be considered. Thus, a fully theoretical simulation that can be precisely and directly compared with experimental observations in both desorption and diffusion is still lacking.

In this report, the kinetic properties of various hydrogen-isotope (H, D, and T) monomers were simulated by means of a composite method consisting of density functional theory (DFT),<sup>23</sup> density functional perturbation theory (DFPT),<sup>24</sup> and harmonic transition state theory (hTST).<sup>25–28</sup> The kinetic change of the magnetic property of the hydrogenated graphene during the desorption and diffusion of the hydrogen monomer was discussed. The vibrational contribution, including the zero-point energy correction in the activation energy, was considered with hTST. The kinetic properties of various hydrogen-isotope monomers were simulated under conditions of annealing for 10 min and of heating at a constant rate (1.0 K/s).

## II. Methodology

The overbarrier jump frequency between two local minimum states (initial and final states or reactant and product states) can be expressed in the Arrhenius form as<sup>27,29</sup>

$$\nu = \nu^* \exp\left(-\frac{E_{ac}}{k_B T}\right) \quad (1)$$

where  $\nu^*$  is the exponential prefactor and  $E_{ac}$  is the activation energy that is required for the reaction to occur. The activation

<sup>†</sup> PACS numbers: 68.65.Pq, 68.43.Bc, 68.35.Ja.

\* To whom correspondence should be addressed. E-mail: zzeng@theory.issp.ac.cn.

<sup>‡</sup> Chinese Academy of Sciences.

<sup>§</sup> Hefei University of Technology.

energy is defined herein to be the vibrational zero-point energy corrected potential barrier, which is expressed as

$$E_{ac} = \Delta E_p + \frac{1}{2} \sum_{i=1}^{3N-1} \hbar \omega_i^S - \frac{1}{2} \sum_{i=1}^{3N} \hbar \omega_i^I \quad (2)$$

$$= \Delta E_p - \Delta F_{vib}(0)$$

where  $\Delta E_p$  is the potential barrier in the reaction path, which can be obtained from DFT calculations, and  $\omega_i^I$  and  $\omega_i^S$  are the vibrational frequencies of the  $i$ th mode in the initial and saddle-point states, respectively. Correction  $\Delta F_{vib}(0)$  comes from the vibrational zero-point energy difference between the initial and saddle-point states. The total vibrational degrees of freedom are  $3N$ ; an imaginary vibrational mode along the migration coordinate in the saddle-point state is excluded; thus,  $3N - 1$  vibrational modes are considered for the saddle-point state. From quantum mechanically modified hTST, prefactor is expressed as<sup>25,29,30</sup>

$$v_{qm}^* = \frac{k_B T \prod_{i=1}^{3N} \left[ 1 - \exp\left(-\frac{\hbar \omega_i^I}{k_B T}\right) \right]}{h \prod_{i=1}^{3N-1} \left[ 1 - \exp\left(-\frac{\hbar \omega_i^S}{k_B T}\right) \right]} = \frac{k_B T \prod_{i=1}^{3N-1} \exp\left(\frac{\hbar \omega_i^S}{k_B T}\right) \bar{n}_T(\omega_i^S)}{h \prod_{i=1}^{3N} \exp\left(\frac{\hbar \omega_i^I}{k_B T}\right) \bar{n}_T(\omega_i^I)} \quad (3)$$

where  $\bar{n}_T(\omega_i)$  is the bosonic phonon occupation number of the  $i$ th vibrational mode. When the temperature approaches infinity, the classical limit of the prefactor is expressed as

$$v_{cl}^* = \frac{1}{2\pi} \frac{\prod_{i=1}^{3N} \omega_i^I}{\prod_{i=1}^{3N-1} \omega_i^S} \quad (4)$$

This classical-limit form is also the Vineyard's form<sup>26</sup> in which all of the vibrational modes are assumed to be completely thermoactivated. From hTST as described above, the mass-dependent vibrational frequencies are responsible for the difference in kinetic properties of H, D, and T monomers as shown later in this report.

The first-order rate equation for desorption can be expressed as<sup>18,27</sup>

$$\frac{dn(t)}{dt} = -v_{des}(T)n(t) \quad (5)$$

where  $v_{des}$  is the desorption frequency,  $n(t)$  is the residual number of hydrogen monomers on graphene at the  $t$  moment, and  $t = 0$  represents the starting moment for initializing the kinetic movement.

In the annealing process, the temperature is kept constant ( $T = T_0$ ); in that case, the variation of the residual number with respect to time is expressed as

$$n(t) = n(0) \exp[-v_{des}(T_0)t] \quad (6)$$

The diffusion can be described by the mean square displacement ( $\langle |\mathbf{r}(t) - \mathbf{r}(0)|^2 \rangle$ ) of a monomer parallel to graphene. From Fick's second law, we have

$$\langle |\mathbf{r}(t) - \mathbf{r}(0)|^2 \rangle = 2dD_{ad}(T)t \quad (7)$$

where  $d$  is the dimensionality of the diffusion of a hydrogen monomer on graphene (2 here), and  $D_{ad}$  is the diffusion coefficient, which is temperature-dependent and is expressed as<sup>29</sup>

$$D_{ad} = \frac{1}{2d} \Gamma a^2 \quad (8)$$

where  $\Gamma$  is the total jump frequency of the monomer, and  $a$  is the jump length. For the diffusion of a monomer on graphene,  $\Gamma$  here is  $3v_{diff}$  ( $v_{diff}$  is the diffusion frequency), which is combined with the fact that there are three equivalent final sites to which a monomer at an initial site can diffuse, and  $a$  is taken to be the optimized C–C bond length of 1.426 Å. The diffusion radius of the monomer is defined as the square root of the mean square displacement

$$r_{diff} = \sqrt{2dD_{ad}(T)t} \quad (9)$$

which can be used directly to determine whether the hydrogen monomer on graphene is diffusionally mobile.

In the heating process, if the temperature increases at a constant rate  $\alpha$  ( $T = \alpha t$ ), the variation of the residual number with respect to time is expressed as

$$n(t) = n(0) \exp\left[-\int_0^t v_{des}(\alpha t) dt\right] \quad (10)$$

where  $\alpha$  is always 1.0 K/s.<sup>2,16,17</sup> The relative desorption rate is therefore defined by the ratio of the desorption rate to the initial monomer number

$$R_{des}(T, t) = v_{des}(T)n(t)/n(0) \quad (11)$$

which is both time- and temperature-dependent.

In this report, a monolayer of graphene served as a structural model of a graphite surface. This was feasible because the effect of the weak van de Waals interaction between neighboring graphene layers on the chemisorption properties of hydrogen monomer can be neglected; in our DFT tests using local density approximation (LDA) and generalized gradient approximation (GGA), the bilayer-graphene structural model yields potential barriers with a difference less than 8 meV with respect to the monolayer structural model. The lattice constant of graphene has been found to be very close to graphite (within 0.05%) at 200–500 K,<sup>31</sup> which is the most important temperature range for the kinetic movements of the hydrogen monomer as shown below. A hydrogen monomer on a  $5 \times 5$  periodic supercell of graphene (50 C atoms) with a 10 Å vacuum along the direction perpendicular to the surface can be considered as an isolated monomer; our tests show that the interaction between two monomers in two such neighboring supercells can be neglected

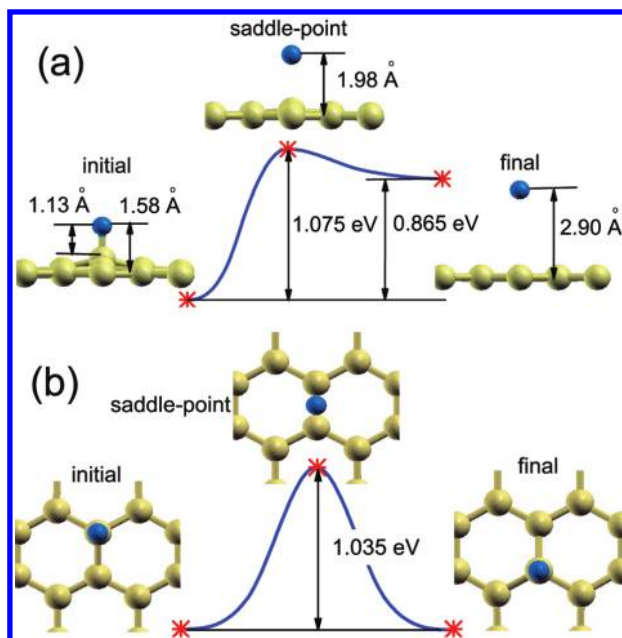


**Figure 1.** MEPs for the (a) desorption and (b) diffusion of a hydrogen monomer on a graphene layer. In the paths, the initial, saddle-point, and final states are labeled with stars, and their structures are shown at the side of the figure. The final state in the desorption MEP is fixed to be the physisorption state. The yellow spheres represent carbon atoms and the smaller blue spheres represent hydrogen atoms.

(see the Supporting Information). This is consistent both with the findings of Shytov<sup>7</sup> on the basis of a theory of electron-mediated interaction and with those of Boukhvalov and Katsnelson<sup>32</sup> on the basis of DFT calculations. The DFT and DFPT calculations were carried out using the Quantum Espresso code package<sup>33</sup> in which the ultrasoft<sup>34</sup> spin-polarized PBE<sup>35</sup> pseudopotentials were used to describe the electronic exchange and correlation energy. The wave function and the charge density were expanded using energy cutoffs of 35 and 350 Ry. For the calculation of electronic density of states (DOS), a  $6 \times 6 \times 1$  uniform  $k$ -point grid with the tetrahedron interpolation scheme<sup>36</sup> was used for the integration of the electronic states over the first Brillouin zone. For the other calculations, a  $4 \times 4 \times 1$  uniform  $k$ -point grid with the Methfessel-Paxton smearing technique<sup>37</sup> was used, where the smearing width was 0.03 Ry. The partial DOS of hydrogen was obtained using the Löwdin population analysis. A force threshold of  $10^{-4}$  Ry/bohr was used for the structural optimization. The reaction paths were described by the minimum energy paths (MEPs) between two local minimum states that were calculated using the climbing-image nudged elastic band method<sup>38</sup> with five images for each reaction path. For calculating the vibrational frequencies, only the gamma point at the Brillouin zone center was selected.

### III. Results and Discussion

The calculated MEPs for the desorption and diffusion processes of a hydrogen monomer are shown in Figure 1 in which the structures of the initial (reactant), saddle-point (transition), and final (product) states are also shown. The final state in the desorption MEP has been fixed to be the physisorption state. To simulate the desorption MEP from the physisorption state to the fully desorbed state, a vacuum with a size larger than 10 Å (e.g., 16.6 Å in ref 3) is needed to completely eliminate any weak interaction between the desorbed hydrogen atom and the graphene layer in the neighboring supercell. However, as seen from the Methodology section, precise

potential surfaces from the chemisorption state to the saddle-point states are enough for the simulation of reaction rates in this report. The energy for the fully desorbed state here is calculated by summing the energies of an isolated hydrogen atom and an isolated graphene layer. In the desorption process shown in Figure 1a, the hydrogen monomer moves away from the graphene layer in the direction perpendicular to the layer. At the first stage of the desorption process (the chemisorption state), the hydrogen atom is at the top site with a height of 1.58 Å bonded to a C atom that protrudes from the graphene plane with a height of 0.45 Å. The calculated protrusion height is somewhat method-dependent, and values ranging from 0.26 to 0.49 Å have been obtained by others.<sup>19,39–44</sup> In the desorption saddle-point state, the hydrogen atom is at the top site with a height of 1.98 Å. The potential barrier was defined as the energy difference between the saddle-point state and the initial state; the calculated desorption potential barrier is 1.075 eV. The final (physisorption) state is 0.865 eV higher in energy than the initial (chemisorption) state; the fully desorbed state is 0.890 eV higher than the initial state and 0.035 eV higher than the physisorption state. The small energy difference of 0.035 eV also indicates that a very large vacuum is needed if one wants to obtain the fully desorbed state in the vacuum. This calculated potential surface along the desorption MEP is very close to Hornekær et al.'s theoretical result,<sup>3</sup> where the smoothly varying potential surface for the MEP from the physisorption state to the fully desorbed state also has been shown. In addition, if the hydrogen monomer climbs over the desorption barrier, it will escape from the graphene layer with high velocity after climbing down the potential barrier. In the diffusion process shown in Figure 1b, the hydrogen atom moves along a C–C bond at an average height of about 1.40 Å. In the diffusion saddle-point state, the hydrogen atom is at the bridge site with a height of 1.20 Å. The diffusion potential barrier is 1.035 eV, which is somewhat smaller than the desorption potential barrier. This potential barrier is insensitive to the supercell size in our calculation (see the Supporting Information), although there has been discussion on this point recently.<sup>45</sup>

The kinetic movement of the hydrogen monomer can result in the kinetic change of the magnetic property of the hydrogenated graphene. Figure 2 shows the electronic DOS of the initial, desorption saddle-point, and diffusion saddle-point states as well as the respective partial DOS of the hydrogen monomer. The initial state and the desorption saddle-point state both have a total magnetic moment of  $1.0 \mu_B$ , while the diffusion saddle-point state is nonmagnetic. The DOS of the initial state is consistent with the theoretical results by others.<sup>20,46</sup> The adsorption of hydrogen atom breaks an aromatic  $\pi$  bond in graphene, which results in one unsaturated C(p) orbital. This unsaturated C(p) orbital is responsible for the two narrow peaks (bands) placed around the Fermi level in the total DOS. The energy gap is 0.245 eV. As seen from the partial DOS of the H(1s) orbital, the contribution from the H(1s) orbital to these two bands is small. The unpaired electron occupying the lower band is responsible for the magnetic moment of  $1.0 \mu_B$ . The energies of the other spin-up bands shift downward a little with respect to their spin-down counterparts because of the exchange-correlation interaction between the electrons in the magnetic C(p) orbital and the other electrons. In the desorption saddle-point state, the partial DOS of the H(1s) orbital is much larger than that in the initial state. This is because the H(1s) orbital is much less hybridized with graphene in the desorption saddle-point state than that in the initial state, and less electrons transfer from H to graphene. Thus, in the desorption process, the



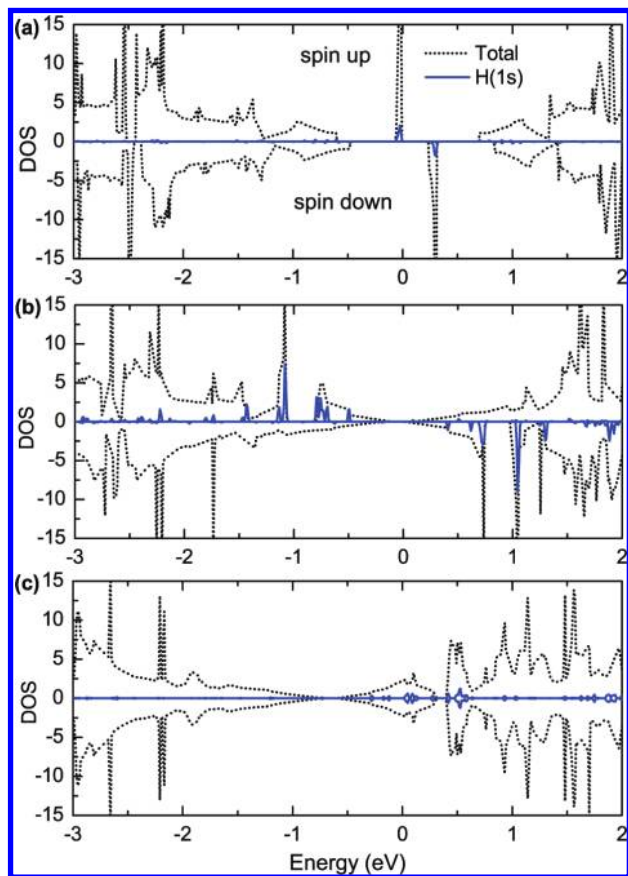


**Figure 2.** The total electronic DOS and the partial DOS of the hydrogen atom of the (a) initial state, (b) desorption saddle-point state, and (c) the diffusion saddle-point state.

contribution of the H(1s) orbital to the total magnetic moment of  $1.0 \mu_B$  will increase up to 100% when the H monomer is fully desorbed. The spin-up bands do not significantly shift with respect to the spin-down ones, which indicates the interaction between the magnetic H atom with graphene is weak. Also, the linear dispersion of the total DOS near the Fermi level is the same as that of graphene indicating that the aromatic  $\pi$  bond in graphene which is broken in the chemisorption state has been restored. In the diffusion saddle-point state, the linear dispersion part of the total DOS is not influenced by the presence of the hydrogen monomer on the bridge site, and the Fermi level shifts upward into the conduction bands. This reveals that the hydrogen monomer does not hybridize with graphene but just dopes graphene with itinerant electrons. This is the reason why the diffusion saddle-point state is nonmagnetic. Thus, in the diffusion process, the total magnetic moment decreases from  $1.0 \mu_B$  down to  $0.0 \mu_B$  when leaving from the chemisorption state to the diffusion saddle-point state.

The displacement of the hydrogen monomer in each eigenvector of the vibrational dynamic matrix was represented by  $\mathbf{e}(\omega_i)$  ( $i$  is the index of the vibrational mode); the calculated spectra of the  $|\mathbf{e}^M(\omega_i)|^2$  ( $M = \text{H, D, and T}$ ) for the initial, desorption saddle-point, and diffusion saddle-point states are shown in Figure 3. The modes with large values of  $|\mathbf{e}(\omega_i)|^2$  are localized stretching (S) and bending (B) modes. The isotope effect in the phonon spectra is obvious in that the vibrational frequency decreases with increasing monomer mass. The stretching modes of H at  $2664 \text{ cm}^{-1}$  and of D at  $1951 \text{ cm}^{-1}$  in the initial state are very close to the experimental measurements of  $2650\text{--}2680 \text{ cm}^{-1}$  and  $1950\text{--}1955 \text{ cm}^{-1}$ .<sup>17,47</sup> In the desorption saddle-point state, the stretching mode of each isotope monomer

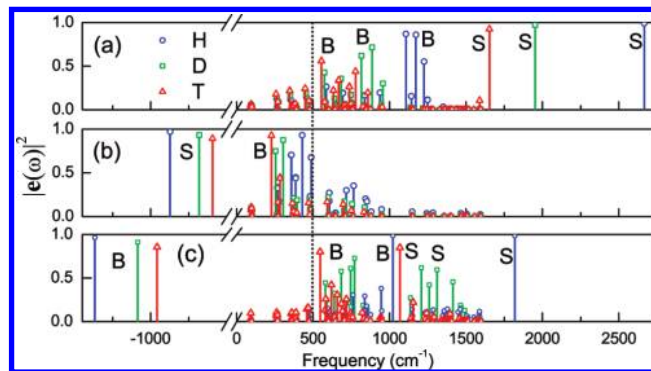


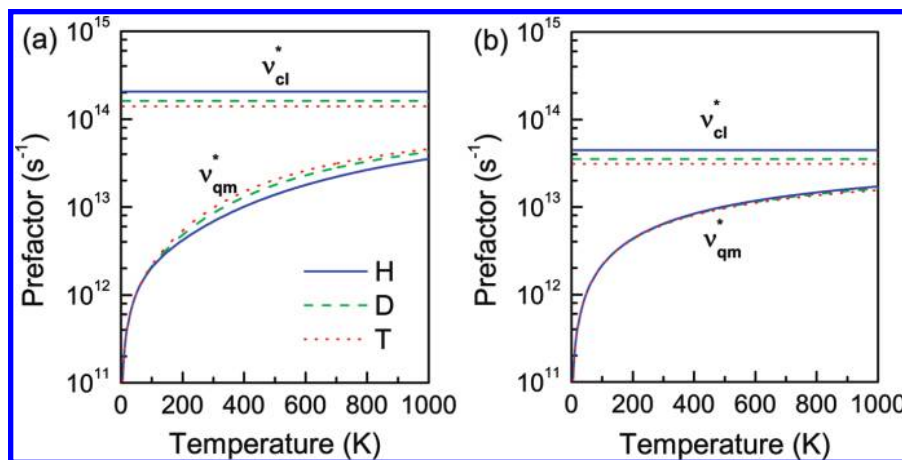
**Figure 3.** The calculated spectra of the  $|\mathbf{e}(\omega_i)|^2$  ( $i$  is the index of the vibrational mode) for the hydrogen-isotope monomers in the (a) initial, (b) desorption saddle-point, and (c) diffusion saddle-point states. The imaginary vibrational modes in the saddle-point states are designated with negative frequencies. S and B represent the stretching and bending modes, respectively. The division of the lower region and higher region (see text) at  $500 \text{ cm}^{-1}$  is labeled by a gray dotted vertical line.

**TABLE 1: Vibrational Zero-Point Energy Corrections ( $\Delta F_{\text{vib}}(0)$ ) in the Activation Energies (in eV) for the Desorption (des.) and Diffusion (dif.) of Hydrogen-Isotope (H, D, and T) Monomers**

	$\Delta F_{\text{vib}}^{\text{H}}(0)$	$\Delta F_{\text{vib}}^{\text{D}}(0)$	$\Delta F_{\text{vib}}^{\text{T}}(0)$
des.	0.205	0.140	0.113
dif.	0.114	0.084	0.072

becomes imaginary, while in the diffusion saddle-point state, one bending mode of each isotope monomer becomes imaginary. The real stretching and bending modes in the diffusion saddle-point state have larger vibrational frequencies than the real bending modes in the desorption saddle-point state; this will result in a difference between the exponential prefactor of desorption and that of diffusion as shown in the next paragraph. For light-mass atoms such as hydrogen isotopes, the vibrational zero-point energy corrections ( $\Delta F_{\text{vib}}(0)$ ) are very important to the precise estimation of activation energies. The calculated  $\Delta F_{\text{vib}}(0)$  values for H, D, and T monomers are listed in Table 1. The values, which range from 0.072 to 0.205 eV, indeed cannot be neglected if the kinetic properties of hydrogen isotope monomers are to be understood. The isotope effect in the  $\Delta F_{\text{vib}}(0)$  values, which shows that  $\Delta F_{\text{vib}}(0)$  decreases with increasing monomer mass, is a result of the isotope effect in the phonon spectra. Both of these isotope effects will result in the presence of an isotope effect in the desorption and diffusion frequencies of hydrogen monomers as shown in the second paragraph below. In addition, the  $\Delta F_{\text{vib}}(0)$  correction for the desorption potential barrier is larger than that for the diffusion potential barrier because of the disappearance of the highest-frequency real stretching modes and the significant lowering of the bending modes in the desorption saddle-point state with respect to those modes in the initial state. However, in the diffusion saddle-point state, only one lower-frequency real bending mode disappears, and the real stretching and bending modes are less affected. The resonant in-band modes (modes with small values of  $|\mathbf{e}(\omega_i)|^2$ ) in these three states are slightly shifted and are nearly independent of the isotopic character of the adatom. The mode with a frequency around  $630 \text{ cm}^{-1}$  observed in experiments is an example of the resonant in-band modes.<sup>17,47</sup>

The exponential prefactors for H, D, and T monomers calculated from the quantum mechanically modified hTST ( $\nu_{\text{qm}}^*$ ) and its classical limit ( $\nu_{\text{cl}}^*$ , the Vineyard form<sup>26</sup>) are shown in



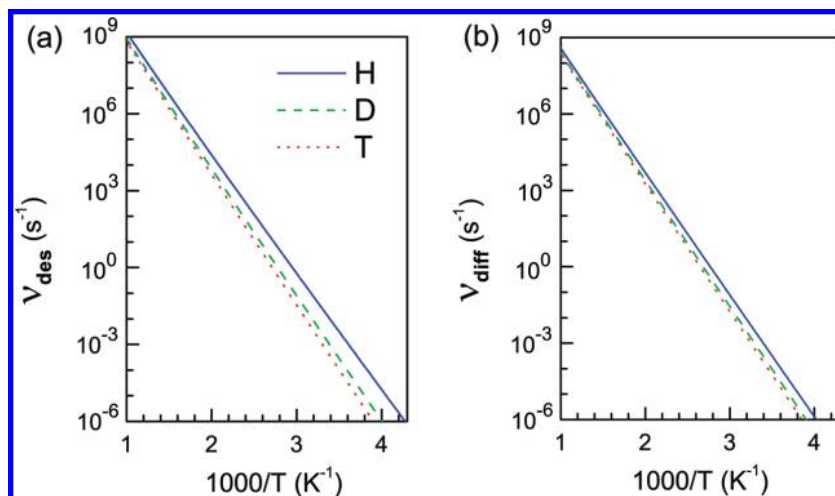
**Figure 4.** Variation of the exponential prefactors with respect to temperature for the (a) desorption and (b) diffusion processes of the hydrogen-isotope monomers on graphene. The values from the quantum mechanically modified hTST ( $\nu_{qm}^*$ ) are compared with their classical-limit values ( $\nu_{cl}^*$ ).

Figure 4. The  $\nu_{cl}^*$ 's are much larger than the corresponding  $\nu_{qm}^*$ 's in the plotted temperature range. Because differences in hydrogen monomer prefactors are mainly determined by the localized stretching and bending modes, the contributions from the high-frequency localized modes are fully considered in the classical-limit hTST (eq 4), while they are much less considered in the quantum mechanically modified hTST because of the weight factors of the bosonic phonon occupation numbers (eq 3). The quantum mechanically modified and the classical-limit prefactors should be equal at very high temperatures. In the classical-limit hTST, all vibrational modes are regarded as completely thermoactivated. In the  $\nu_{cl}^*$ 's, the isotope effect is obvious: the prefactor decreases with increasing monomer mass, which is due to the isotope effect in the phonon spectra in Figure 3 as discussed in the previous paragraph. However, among the quantum mechanically modified desorption prefactors, the relationship  $\nu_{qm}^*(T) > \nu_{qm}^*(D) > \nu_{qm}^*(H)$  holds, and the isotope effect is reversed with respect to the isotope effect in the  $\nu_{cl}^*$ 's. The values of the quantum mechanically modified diffusion prefactors for H, D, and T monomers are nearly the same over a very wide temperature range (0–1000 K). This can be understood from eq 3 and the phonon spectra in Figure 3. For convenience, the phonon spectra are divided into lower and higher regions below and above 500  $\text{cm}^{-1}$ , respectively. In the initial state, all the localized modes are in the higher region. The real localized bending modes in the desorption saddle-point state are significantly lowered such that they now fall within the lower region, while the real localized modes in the diffusion saddle-point state remain in the higher region. In the plotted temperature range, the  $\nu_{qm}^*$ 's are mainly determined by the vibrational modes in the lower region because of the large bosonic phonon occupation numbers of these modes. In the phonon spectra of the initial and diffusion saddle-point state, the lower region contains only the resonant in-band modes, which are nearly independent of the isotopic character of the monomer, therefore, the  $\nu_{qm}^*$ 's for H, D, and T monomers in diffusion are nearly the same. However, in the phonon spectra of the desorption saddle-point state, the low-lying localized bending modes are significantly occupied by phonons at temperatures above 100 K; in this state, the localized modes for the T monomer are the lowest and should be occupied by most phonons and are most readily thermoactivated followed by the modes for D and H monomers in that order. This order of thermoactivation leads to the relative magnitude order of the  $\nu_{qm}^*$ 's for H, D, and T monomers at temperatures above 100 K;

however, this magnitude order will be progressively altered as the temperature increases to high values (not shown) finally achieving the same order as  $\nu_{cl}^*$ 's.

The desorption frequencies ( $\nu_{des}$ ) and diffusion frequencies ( $\nu_{diff}$ ) for the hydrogen-isotope monomers are shown in Figure 5, where the  $\nu_{qm}^*$  is used as the prefactor. Both  $\nu_{des}$  and  $\nu_{diff}$  decrease with increasing monomer mass. This isotope effect is due to the isotope effect in the vibrational zero-point energy correction as shown in Table 1. The  $\nu$  is exponentially dependent on the activation energy and linearly dependent on the  $\nu_{qm}^*$ ; thus, the small reversed isotope effect in the  $\nu_{qm}^*$ 's for the desorption (Figure 4a) does not compete with the normal isotope effect in the zero-point energy corrections. For each isotope, the desorption frequencies are larger than the corresponding diffusion frequencies because the desorption activation energy is less than the diffusion activation energy from eq 2. Additionally, the desorption prefactor is also larger than the diffusion prefactor. At room temperature (298 K), the  $\nu_{diff}$ 's for H, D, and T monomers are  $1.6 \times 10^{-3}$ ,  $4.8 \times 10^{-4}$ , and  $3.0 \times 10^{-4} \text{ s}^{-1}$ , respectively; the  $\nu_{des}$ 's are  $1.4 \times 10^{-2}$ ,  $1.4 \times 10^{-3}$ , and  $5.5 \times 10^{-4} \text{ s}^{-1}$ , respectively.

After several hydrogen monomers are deposited onto a graphene or graphite surface and if the system is annealed at a constant temperature  $T_0$  for a time interval  $t_0$ , the monomers are desorbed from the surface or diffuse away from the initial site. The kinetic properties of hydrogen monomers under this annealing condition were simulated by eqs 6 and 9 with  $t_0$  being 10 min (600 s) in accordance with Hornekær et al.'s experiment.<sup>3</sup> Figure 6a shows the variations of the relative residual monomer number ( $n(t_0)/n(0)$ ) and the diffusion radius ( $r_{diff}$ ) with respect to  $T_0$ . The curves of  $n(t_0)/n(0)$  and  $r_{diff}$  present an isotope effect that a hydrogen monomer of lower mass is desorbed from the surface and diffuses on the surface more easily. During a 10 min annealing, significant desorption does not occur in our simulation until  $T_0 > 250 \text{ K}$ . However, the monomers are nearly completely desorbed at  $T_0 > 294 \text{ K}$  for H, at  $T_0 > 312 \text{ K}$  for D, and at  $T_0 > 320 \text{ K}$  for T. Although the  $r_{diff}$  (600 s) increases rapidly with  $T_0$ , the monomers (H, D, and T) on the graphene should be diffusively immobile at any  $T_0$  because the diffusion radius for each hydrogen-isotope monomer is very short at temperatures below the complete-desorption temperature above which there will be no residual monomer left for measurement. This type of diffusional immobility matches experimental measurements obtained on D monomers.<sup>3,18</sup> The annealing process of D monomers on graphene at 298 K is visualized in



**Figure 5.** Variation of the (a) desorption frequencies ( $\nu_{\text{des}}$ ) and (b) diffusion frequencies ( $\nu_{\text{diff}}$ ) of hydrogen-isotope monomers from the quantum mechanically modified hTST with respect to the inverse of temperature.

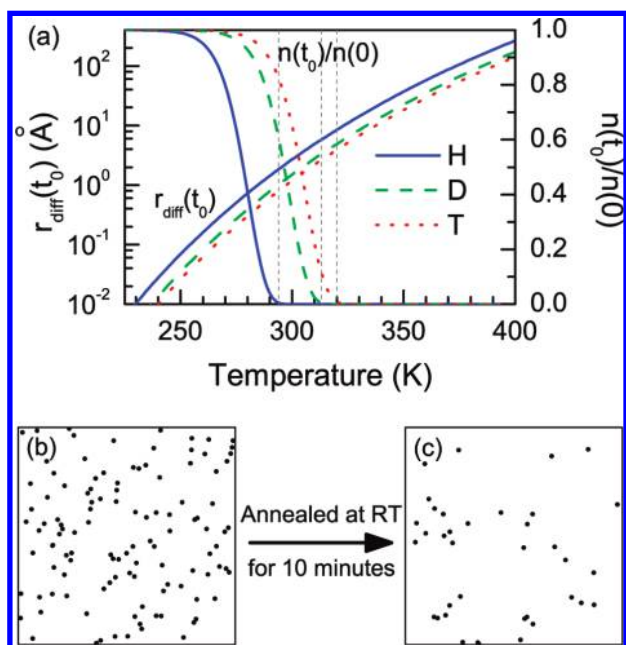


**Figure 6.** (a) Variation of the diffusion radius and the relative residual monomer number with respect to the annealing temperature ( $t_0 = 600$  s). The three gray dashed vertical lines at the complete-desorption temperatures of H, D, and T monomers (294, 312, and 320 K, respectively) are intended as a visualization tool. (b, c) The visualization of the annealing process in a for D monomers at room temperature (298 K) for 10 min. The area of the graphene surface is  $100 \text{ nm} \times 100 \text{ nm}$ , and the initial coverage is set to 0.03% ( $n(0) = 114$ ) according to the experiment in ref 3.

Figure 6b and c to compare with Hornekær et al.'s experiment in ref 3. In accordance with this experiment, the initial coverage (monomer number) is set to 0.03% ( $n(0) = 114$  in a  $100 \text{ nm} \times 100 \text{ nm}$  surface area) (Figure 6b). After 10 min, only 33% of the monomers remain on graphene, a value that is comparable to the 20% observed in Hornekær's experiment.  $n(t_0)/n(0)$  exponentially decreases with temperature, and the value of 20% corresponds to the annealing temperature of 301 K in this simulation. The discrepancy between simulation and experiment may arise from the fact that a small fraction of the monomers will be desorbed during the heating and cooling steps in the annealing process; the effect of scanning tunneling microscopy (STM) measurement will also result in additional desorption

of hydrogen monomers, which is not considered in this simulation; the interlayer interaction makes the hydrogen monomers easier to escape from graphite surface in experiments. As mentioned in the Methodology section, the interlayer interaction in bilayer graphene will lower the potential barriers by about 8 meV. This is because the bilayer graphene is less flexible than the monolayer graphene,<sup>32</sup> which makes the monolayer graphene more reactive to bond with the hydrogen monomer. If a correction of  $-8$  meV is considered in the desorption activation energy,  $n(t_0)/n(0)$  equals 20% at 299 K. Thus, the interlayer interaction just results in a temperature difference of a couple of Kelvins, which indicates its weak effect on the kinetic properties of the hydrogen monomer and supports the validity of the monolayer structural model used in this report.

In some experimental measurements of kinetic properties, the temperature is increased at a constant rate ( $\alpha$ ). The kinetic properties of hydrogen monomers under this constant-rate heating condition were simulated by eqs 10 and 11 with  $\alpha$  as 1.0 K/s. From eq 11, the relative desorption rate ( $R_{\text{des}}(T, t)$ , Figure 7a) is determined both by the desorption frequency ( $\nu_{\text{des}}(T)$ ) and by the residual monomer number ( $n(t)$ ). On heating,  $\nu_{\text{des}}(T)$  increases with temperature or elapsed time (Figure 5) and  $n(t)$  decreases (Figure 7b); thus, there will be a desorption peak for each hydrogen-isotope monomer in the desorption spectrum of  $R_{\text{des}}$ . The desorption peak for the H monomer is at 316 K, the desorption peak for the D monomer is at 336 K, and the desorption peak for the T monomer is at 344 K. In the desorption spectra, an isotope effect can be seen that a hydrogen monomer of lower mass is desorbed from the surface more easily, which is the same as the isotope effect in the annealing process. The same as discussed in the previous paragraph, the weak interlayer interaction will only make the desorption spectra move to low temperatures by about 2 K.

In addition, when the coverage of hydrogen atoms on graphene increases, hydrogen dimers will form and dominate on the surface.<sup>2,16,17</sup> In the desorption spectra under constant-rate heating (1.0 K/s), there are two peaks at 445 (490) K and 560 (580) K for H (D) dimers, which is totally different from the desorption spectra of H (D) monomer in Figure 7. The kinetic properties of hydrogen dimers on graphene and the effect of dimer–dimer interaction have been investigated by us using nearly the same method, which will appear in a forthcoming paper. Generally, the isotope effects, the localization nature of the vibrations of hydrogen dimers, and the dependence of the



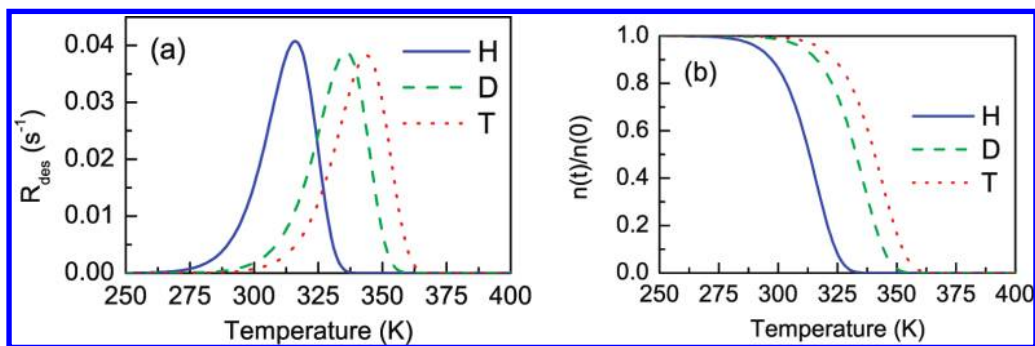


**Figure 7.** (a) Simulated thermal desorption spectra for hydrogen-isotope monomers with the heating rate  $\alpha = 1.0$  K/s. (b) The residual monomer number during the thermal desorption.

kinetic properties on the localized modes are the same as those of the hydrogen monomer. This means that the investigation on the kinetic properties of hydrogen monomer on graphene is instructive to other more complex situations.

#### IV. Conclusions

The kinetic properties of hydrogen-isotope (H, D, and T) monomers on graphene were simulated using a composite ab initio method consisting of density functional theory, density functional perturbation theory, and harmonic transition state theory. The simulations were based on the potential barriers calculated from DFT and on the phonon spectra calculated from DFPT, which were used together to analyze calculated vibrational zero-point energy corrections, exponential prefactors (quantum mechanically modified and classical-limit), jump frequencies, and simulated kinetic properties. The chemisorption state and the desorption saddle-point state both have a magnetic moment of  $1.0 \mu_B$ , while the diffusion saddle-point state is nonmagnetic. From the electronic DOS analysis, in the desorption process, the hybridization of the hydrogen monomer with graphene is reduced and the contribution of the H(1s) orbital to the total magnetic moment increases. In the diffusion process, when leaving from the chemisorption state to the diffusion saddle-point state, this hybridization also decreases; the transferred electrons from H to graphene become more and more itinerant; the total magnetic moment decreases from  $1.0 \mu_B$  down to  $0.0 \mu_B$ . The spectra of the localized vibrational modes of hydrogen are hydrogen-mass-dependent, which results in the isotope effects in the kinetic properties (prefactor, activation energy, jump frequency, desorption rate, and diffusion radius) of H, D, and T monomers. The zero-point energy correction decreases with increasing monomer mass and is larger for desorption than for diffusion. This results in the isotope effect that a hydrogen monomer of lower mass is desorbed and diffuses more easily (with lower activation energies) and in that the desorption frequency of each hydrogen-isotope monomer is larger than its diffusion frequency. In the simulated 10 min annealing of hydrogen-isotope monomers on graphene, the monomers are quite diffusionally immobile at temperatures lower than the complete-desorption temperature, and a large fraction (67%) of the D monomers on graphene will be desorbed at the annealing temperature of 298 K. These theoretical results are very close to those obtained by experimental observations of hydrogen adatoms on graphite surfaces.<sup>3,18</sup> The thermal desorption spectra ( $\alpha = 1.0$  K/s) of the hydrogen-isotope monomers have also been simulated. The resulting desorption peak for H is at 316 K, for D is at 336 K, and for T is at 344 K. The precise simulation of the kinetic properties of the hydrogen-isotope monomers on graphene described in this report

can help to further precise studies of more complex hydrogenation processes. The precise theoretical predictions for radioactive tritium adatoms are especially useful because it is dangerous to conduct experiments on them in conventional laboratories.

**Acknowledgment.** L.F.H. wishes to thank Liv Hornekær and K. Toyoura for helpful e-mail exchanges. This work was supported by the special Funds for Major State Basic Research Project of China (973) under grant No. 2007CB925004, 863 Project, Knowledge Innovation Program of Chinese Academy of Sciences, and by Director Grants of CASHIPS. Part of the calculations were performed at the Center of Computational Science of CASHIPS and at the Shanghai Supercomputer Center.

**Supporting Information Available:** The variation of the desorption and diffusion barriers with respect to the supercell size. This material is available free of charge via the Internet at <http://pubs.acs.org>.

#### References and Notes

- (1) Coey, J. M. D.; Venkatesan, M.; Fitzgerald, C. B.; Douvalis, A. P.; Sanders, I. S. *Nature* **2002**, *420*, 156.
- (2) Hornekær, L.; Šljivančanin, Ž.; Xu, W.; Otero, R.; Rauls, E.; Stensgaard, I.; Lægsgaard, E.; Hammer, B.; Besenbacher, F. *Phys. Rev. Lett.* **2006**, *96*, 156104.
- (3) Hornekær, L.; Rauls, E.; Xu, W.; Šljivančanin, Ž.; Otero, R.; Stensgaard, I.; Lægsgaard, E.; Hammer, B.; Besenbacher, F. *Phys. Rev. Lett.* **2006**, *97*, 186102.
- (4) Ferro, Y.; Marinelli, F.; Allouche, A. *Chem. Phys. Lett.* **2003**, *368*, 609.
- (5) Morris, J. *Nature* **2003**, *422*, 674.
- (6) Lachawiec, A. J., Jr.; Qi, G.; Yang, R. T. *Langmuir* **2005**, *21*, 11418.
- (7) Shytov, A. V.; Abanin, D. A.; Levitov, L. S. *Phys. Rev. Lett.* **2009**, *103*, 016806.
- (8) Ryu, S.; Han, M. Y.; Maultzsch, J.; Heinz, T. F.; Kim, P.; Steigerwald, M. L.; Brus, L. E. *Nano Lett.* **2008**, *8*, 4597.
- (9) Elias, D. C.; Nair, R. R.; Mohiuddin, T. M. G.; Morozov, S. V.; Blake, P.; Halsall, M. P.; Ferrari, A. C.; Boukhvalov, D. W.; Katsnelson, M. I.; Geim, A. K.; Novoselov, K. S. *Science* **2009**, *323*, 610.
- (10) Sofo, J. O.; Chaudhari, A. S.; Barber, G. D. *Phys. Rev. B* **2007**, *75*, 153401.
- (11) Balog, R.; Jorgensen, B.; Wells, J.; Lægsgaard, E.; Hofmann, P.; Besenbacher, F.; Hornekær, L. *J. Am. Chem. Soc.* **2009**, *131*, 8744.
- (12) Bostwick, A.; McChesney, J.; Emtsev, K. V.; Seyller, T.; Horn, K.; Kevan, S. D.; Rotenberg, E. *Phys. Rev. Lett.* **2009**, *103*, 056404.
- (13) Guisinger, N. P.; Rutter, G. M.; Crain, J. N.; First, P. N.; Stroscio, J. A. *Nano Lett.* **2009**, *9*, 1462.
- (14) Luo, Z.; Yu, T.; Kim, K.; Ni, Z.; You, Y.; Lim, S.; Shen, Z. *ACS Nano* **2009**, *3*, 1781.
- (15) Lebègue, S.; Klintonberg, M.; Eriksson, O.; Katsnelson, M. I. *Phys. Rev. B* **2009**, *79*, 245117.
- (16) Zecho, T.; Güttler, A.; Küppers, J. *Carbon* **2004**, *42*, 609.
- (17) Zecho, T.; Güttler, A.; Sha, X.; Jackson, B.; Küppers, J. *J. Chem. Phys.* **2002**, *117*, 8486.
- (18) Baouche, S.; Gamborg, G.; Petrunin, V. V.; Luntz, A. C.; Baurichter, A. *J. Chem. Phys.* **2006**, *125*, 084712.

- (19) Ferro, Y.; Marinelli, F.; Jelea, A.; Allouche, A. *J. Chem. Phys.* **2004**, *120*, 11882.
- (20) Casolo, S.; Løvvik, O. M.; Martinazzo, R.; Tantardini, C. F. *J. Chem. Phys.* **2009**, *130*, 054704, and references therein.
- (21) Herrero, C. P.; Ramírez, R. *Phys. Rev. B* **2009**, *79*, 115429.
- (22) Roman, T.; DiNo, W. A.; Nakanishi, H.; Kasai, H.; Sugimoto, T.; Tange, K. *Jpn. J. Appl. Phys.* **2006**, *45*, 1765.
- (23) Kohn, W.; Sham, L. J. *Phys. Rev.* **1965**, *140*, A1133.
- (24) Baroni, S.; de Gironcoli, S.; Dal Corso, A.; Giannozzi, P. *Rev. Mod. Phys.* **2001**, *73*, 515.
- (25) Eyring, H. *J. Chem. Phys.* **1935**, *3*, 107.
- (26) Vineyard, G. H. *J. Phys. Chem. Solids* **1957**, *3*, 121.
- (27) Hänggi, P.; Talkner, P.; Borkovec, M. *Rev. Mod. Phys.* **1990**, *62*, 251.
- (28) Pollak, E.; Talkner, P. *Chaos* **2005**, *15*, 026116.
- (29) Toyoura, K.; Koyama, Y.; Kuwabara, A.; Oba, F.; Tanaka, I. *Phys. Rev. B* **2008**, *78*, 214303.
- (30) Sundell, P. G.; Björketun, M. E.; Wahnström, G. *Phys. Rev. B* **2007**, *76*, 094301.
- (31) Mounet, N.; Marzari, N. *Phys. Rev. B* **2005**, *71*, 205214.
- (32) Boukhvalov, D. W.; Katsnelson, M. I. *J. Phys.: Condens. Matter* **2009**, *21*, 344205.
- (33) Giannozzi, P. *J. Phys.: Condens. Matter* **2009**, *21*, 395502.
- (34) Vanderbilt, D. *Phys. Rev. B* **1990**, *41*, R7892.
- (35) Perdew, J. P.; Burke, K.; Ernzerhof, M. *Phys. Rev. Lett.* **1996**, *77*, 3865.
- (36) Blöchl, P. E.; Jepsen, O.; Anderson, O. K. *Phys. Rev. B* **1994**, *49*, 16223.
- (37) Methfessel, M.; Paxton, A. T. *Phys. Rev. B* **1989**, *40*, 3616.
- (38) Henkelman, G.; Uberuage, B. P.; Jónsson, H. *J. Chem. Phys.* **2000**, *113*, 9901.
- (39) Miura, Y.; Kasai, H.; Dino, W.; Nakanishi, H.; Sugimoto, T. *J. Appl. Phys.* **2003**, *93*, 3395.
- (40) Boukhvalov, D. W.; Katsnelson, M. I.; Lichtenstein, A. I. *Phys. Rev. B* **2008**, *77*, 035427.
- (41) Ferro, Y.; Teillet-Billy, D.; Rougeau, N.; Sidis, V.; Morisset, S.; Allouche, A. *Phys. Rev. B* **2008**, *78*, 085417.
- (42) Kerwin, J.; Jackson, B. *J. Chem. Phys.* **2008**, *128*, 084702.
- (43) Dennis, P. A.; Iribarne, F. J. *Mol. Struct. (THEOCHEM)* **2009**, *907*, 93.
- (44) Ao, Z. M.; Peeters, F. M. J. *Phys. Chem. C* **2010**, *114*, 14503.
- (45) Boukhvalov, D. W. *Phys. Chem. Chem. Phys.* **2010**, *12*, 15367.
- (46) Duplock, E. J.; Scheffler, M.; Lindan, P. J. D. *Phys. Rev. Lett.* **2004**, *92*, 225502.
- (47) Allouche, A.; Ferro, Y.; Angot, T.; Thomas, C.; Layet, J. M. *J. Chem. Phys.* **2005**, *123*, 124701.

JP109160C